ADVANCED ENERGY MATERIALS
www.advenergymat.de

Hierarchically Porous and Minimally Stacked Graphene Cathodes for High-Performance Lithium–Oxygen Batteries

Wei Yu, Zhaohan Shen, Takeharu Yoshii, Shinichiroh Iwamura, Manai Ono, Shoichi Matsuda, Makoto Aoki, Toshihiro Kondo, Shin R. Mukai, Shuji Nakanishi, and Hirotomo Nishihara**

Although lithium–oxygen batteries have attracted attention due to their extremely high energy densities, rational design, and critical evaluation of high-energy-density cathode for practical Li–O_2 batteries is still urgently needed. Herein, the multiscale, angstrom-to-millimeter, precisely controllable synthesis of binder-free cathodes with minimally stacked graphene free from edge sites is demonstrated. The proposed Li–O_2 battery, based on a hierarchically porous cathode with a practical mass loading of >4.0 mg cm^{-2}, simultaneously exhibits an unprecedented specific areal (>30.0 mAh cm^{-2}), mass (>6300 mAh g^{-1}), and volumetric (>480 mAh cm^{-3}) capacities. The battery displays the optimal energy density of 793 Wh kg^{-1} critically normalized to the total mass of all active materials including electrolytes and even discharge products Li_2O_2. Comprehensive in situ characterizations demonstrate a unique discharge mechanism in hierarchical pores which contributes to competitive battery performance. Superior rate performance in a current density range of 0.1 to 0.8 mA cm^{-2} and long-cycle stability (>260 cycles) at a current density of 0.4 mA cm^{-2}, outperforming state-of-the-art carbon cathodes. This study yields insight into next-generation carbon cathodes, not only for use in practical Li–O_2 batteries, but also in other metal–gas batteries with high energy densities.

1. Introduction

Next-generation energy storage and conversion technologies are urgently required to satisfy development goals via large-scale power grids, electric vehicles, and portable electronics.[1] Lithium–oxygen (Li–O_2) batteries attract considerable attention because of their high theoretical energy densities.[2] A Li–O_2 battery typically comprises a Li metal anode, liquid/solid electrolyte, and porous cathode. Several types of discharge products exist, such as lithium superoxide (LiO_2),[3] lithium hydroxide (LiOH),[4] and lithium oxide (Li_2O),[5] but the most typical discharge product in non-aqueous Li–O_2 batteries is lithium peroxide (Li_2O_2). An extremely high energy density (3500 Wh kg^{-1}) maybe realized via the oxygen reduction/evolution reactions corresponding to Li_2O_2 formation/decomposition during discharging and charging.[6] However, the sluggish

---

W. Yu, S. Iwamura, H. Nishihara
Advanced Institute for Materials Research (WPI-AIMR)
Tohoku University
Sendai 980-8577, Japan
E-mail: yu.wei.a3@tohoku.ac.jp; hirotomo.nishihara.b1@tohoku.ac.jp

Z. Shen, T. Yoshii, H. Nishihara
Institute of Multidisciplinary Research for Advanced Materials
Tohoku University
Sendai 980-8577, Japan

S. Iwamura
3DC Inc.
Sendai 980-8577, Japan

M. Ono, S. Matsuda
Center for Green Research on Energy and Environmental Materials
National Institute for Material Science
Tsukuba, Ibaraki 305-0044, Japan

S. Matsuda
NIMS-SoftBank Advanced Technologies Development Center
National Institute for Material Science
Tsukuba, Ibaraki 305-0044, Japan

M. Aoki, T. Kondo
Graduate School of Humanities and Sciences
Ochanomizu University
Tokyo 112-8610, Japan

S. R. Mukai
Faculty of Engineering
Hokkaido University
Sapporo 060-6828, Japan

S. Nakanishi
Research Center for Solar Energy Chemistry
Graduate School of Engineering Science
Osaka University
Toyonaka, Osaka 560-8531, Japan

The ORCID identification number(s) for the author(s) of this article can be found under https://doi.org/10.1002/aenm.202303055

DOI: 10.1002/aenm.202303055

kinetics of the formation/decomposition of electrically insulated Li_2O_2 result in a large overpotential, low capacity, and limited cycle life.[7] Recently, significant efforts were directed toward investigating the reaction mechanism.[8] Considerable progress has been reported in reducing the overpotential and extending the battery life by using protected Li anodes,[9] stable electrolytes,[10] efficient solid/soluble catalysts,[11] and robust porous cathodes.[12] However, few studies focus on energy density improvements using practical cathodes with large mass loadings (>4.0 mg cm^{-2}),[13] a crucial aspect in commercializing Li–O_2 batteries with high device energy densities (>500 Wh kg^{-1}).[14]

As the formation, storage, and decomposition of Li_2O_2 on the cathode directly determine the battery's specific capacity and discharge/charge potential of the battery, a well-designed cathode is crucial in a practical Li–O_2 battery.[15] Carbon materials are commonly used as cathodes in Li–O_2 batteries owing to their relatively large surface areas, high conductivities, and abundant pores. However, the areal densities of carbon cathodes in most previous studies are <1.0 mg cm^{-2}.[16] Even if the battery reaches a very high mass capacity of >10 000 mAh g^{-1}, the actual areal capacity is still less than the target areal capacity of 12 mAh cm^{-2}, which is required for a low cost per usable energy (<$100 per kWh).[13b,14] A thick carbon cathode (>500 μm) with a high areal loading (>4 mg cm^{-2}) is necessary for a high areal capacity (>12 mAh cm^{-2}). However, the specific mass capacity is inversely related to the thickness of the carbon cathode because of the significant internal resistance and poor Li^+ and O_2 mass transportation.[17] An ultra-thick cathode (>1 cm) generally exhibits a low volumetric capacity (<200 mAh cm^{-3}),[18] which is rarely discussed in previous studies. The challenge in preparing carbon cathodes with satisfactory performances is due to the strong anisotropy of graphene, which is the primary unit of carbon materials hindering precise structural control over a wide size scale from angstroms to sub-millimeters.[19] Therefore, to meet the criteria of an ideal carbon (**Figure 1a**) for a high energy density Li–O_2 battery, the following characteristics should be achieved: 1) Minimally stacked graphene walls, which provide more active sites and higher specific capacity in grams; 2) Hierarchical structure, in which the micro/mesopores promote the mass transfer of Li^+ and the nucleation of intermediates (LiO_2), and the macropores benefit the mass transfer of O_2 and the growth of discharge products; 3) Free of carbon edge sites and organic binder, which improves the stability of carbon cathodes.

Herein, we propose a new concept for ideal carbon cathode design: a hierarchical porous membrane composing graphene walls without stacking or carbon edge sites prepared via chemical vapor deposition (CVD), followed by high-temperature annealing. We fabricated a prototype cathode by integrating graphene mesosponge (GMS)[20] into a binder-free sheet, with the product denoted GMS-sheet. The multiscale-controllable GMS-sheet with an areal mass (5.0 mg cm^{-2}) exhibited extremely high areal, mass, and volumetric capacities in Li–O_2 batteries, corresponding to a remarkable energy density of 793 Wh kg^{-1} based on all active materials. Moreover, the cycle performance was stable under a current density of 0.4 mA cm^{-2} and a limited capacity of 4.0 mAh cm^{-2}. Therefore, the GMS-sheet is a promising cathode for high-energy-density Li–O_2 batteries and other sustainable energy storage devices, such as Na, K, and Zn–air batteries for application in a post Li-ion battery era.[21]

2. Results and Discussion

2.1. Synthesizing and Optimizing Hierarchically Porous Carbon Cathodes

Figure 1b illustrates the synthesis of a hierarchically porous GMS-sheet cathode with graphene walls without significant stacking or edge sites. Al_2O_3 powder with an average particle size of 7 nm (Figure S1, Supporting Information) is pelletized using a graphite mold (Figure S2, Supporting Information) at 100 N (0.75 MPa) for 5 s (Figure 1c). Then, as-prepared white Al_2O_3-sheets (ϕ 13.0 mm, Figure 1d, Left) are subjected to CVD, using CH_4 as the carbon source, at 900 °C to coat the surfaces of the Al_2O_3 nanoparticles with an extremely thin carbon layer.[20] The graphene stacking can be precisely controlled by the specific catalysis of oxygen vacancies generated on the surface of the oxide template at the initial in situ catalyst-activation step.[22] As carbon-coated Al_2O_3 can be considered a composite of carbon mesosponge (CMS)[20] and Al_2O_3, the resulting black samples (Figure 1d, Middle) are denoted CMS-Al_2O_3-sheets. As we pelletized the Al_2O_3 nanoparticles to form a 3D framework on the millimeter scale, the graphene-wall framework loaded on the Al_2O_3 nanoparticles is also spread over the millimeter scale. The thicknesses and porosities of the Al_2O_3-sheets could be easily controlled via pelletization forces in the range 50–10000 N (Figure S3 and Table S1, Supporting Information). The carbon loading on the CMS-Al_2O_3-sheets, as measured via thermogravimetry (TG, Figure S4, Supporting Information), is ≈28 wt.%, corresponding to an average graphene-stacking number of 2.8.[20] Pure-carbon CMS-sheets are prepared by removing the Al_2O_3 template via HF etching, based on the observation of only broad carbon 002 and 10 peaks in the X-ray diffraction (XRD) pattern (Figure S5, Supporting Information). Finally, a binder-free GMS-sheet (Figure 1d, Right) is fabricated via high-temperature annealing (1800 °C) to remove the edge sites and improve the qualities of the graphene frameworks (Figure S6, Supporting Information).

The structure of the GMS-sheets can be controlled at the angstrom (graphene-stacking number and carbon edge sites), nanometer (spherical mesopores derived from Al_2O_3 nanoparticles), micrometer (microporosity controlled by a pelletization force), and millimeter (thickness and diameter of a GMS-sheet) scales (Figure 1b). Accordingly, the crucial synthetic parameters are the pelletization force (x [N]), amount of Al_2O_3 template (y [mg]), and duration of CVD (z [h]), and the GMS-sheets synthesized under different conditions are denoted as xN-$y$mg-zh-GMS-sheets. As shown in the cross-sectional scanning electron microscopy (SEM) image (**Figure 2a**), the 100N-20mg-4.0h-

S. Nakanishi
Innovative Catalysis Science Division
Institute for Open and Transdisciplinary Research Initiatives (ICS-OTRI)
Osaka University
Suita, Osaka 565-0871, Japan

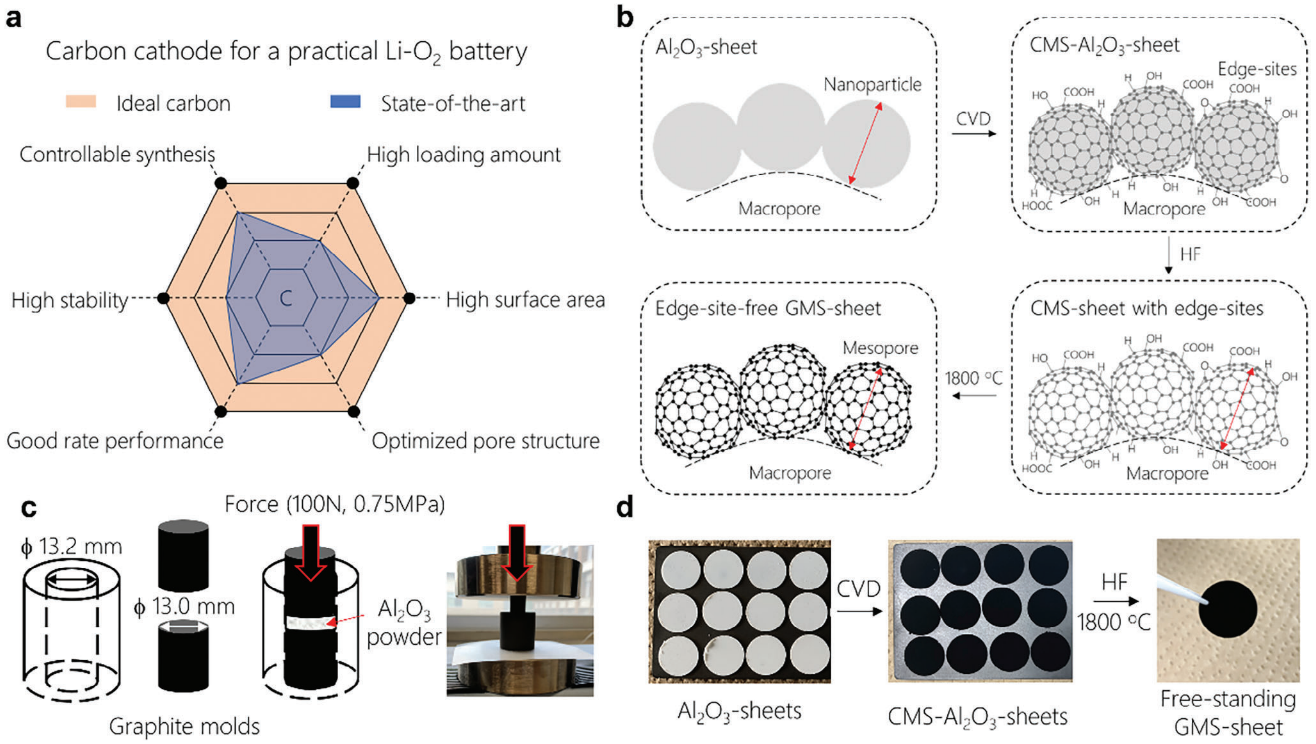

Figure 1. Schematic diagram and synthesis of the ideal carbon cathode. a) Radar chart of ideal carbon cathode requirements and state-of-the-art achievements. b) Schematic illustration of GMS-sheet synthesis process. c) Schematic of the Al_2O_3 pelletization process. A graphite mold with an inner diameter of 13.2 mm and two graphite rods with a diameter of 13.0 mm were used. d) Digital photos of Al_2O_3-sheets before CVD, CMS-Al_2O_3-sheets after CVD, and a free-standing GMS-sheet after the HF and high-temperature treatments.

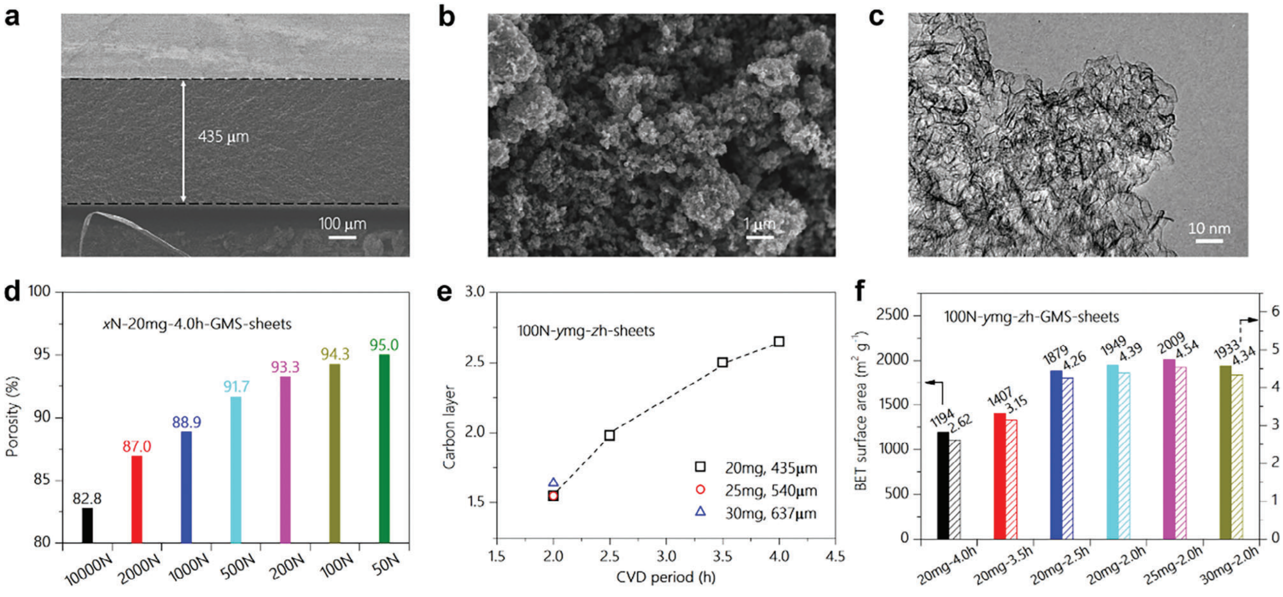

Figure 2. Structural controllability of the GMS-sheet. a—c) Micrographs of the 100N-20mg-4.0h-GMS-sheet. Cross–sectional SEM images at a) low and b) high magnifications. c) A TEM image. d) Total porosities of GMS-sheets synthesized under different pelletization forces varied from 50 to 10 000 N. The same Al_2O_3 amount (20 mg) and duration of CVD (4.0 h) were used in preparing the GMS-sheets. e) Relationship between the CVD durations and average graphene-stacking numbers of the GMS-sheets prepared using different amounts of Al_2O_3. f) Specific surface areas and V_{N2} values of GMS-sheets shown in e. V_{N2} is the sum of the micro- and mesopore volumes calculated from $P/P_0 = 0.96$, as shown in Figure S12 (Supporting Information).

GMS-sheet is a uniform self-standing membrane with a thickness of ≈435 µm. The thickness, which depends on x [N] and y [mg], is controllable between 127 and 637 µm (Figures S7 and S8, Supporting Information). The high-magnification SEM image (Figure 2b) shows the presence of macropores between the aggregates of the spherical nanoparticles. In comparison, the transmission electron microscopy (TEM) image (Figure 2c) shows a nanobubble-like mesoporous framework derived from the Al_2O_3 template (Figure S1, Supporting Information). The developed meso- and macropores can also be confirmed based on N_2 ad-/desorption isotherms (Figure S9, Supporting Information), showing a large hysteresis and the successive N_2 uptake above $P/P_0 = 0.9$. The xN-20mg-4.0h-GMS-sheets display similar N_2 adsorption isotherms at P/P_0<0.8, mesoporous size distributions of <10 nm, and the Brunauer–Emmett–Teller (BET) specific surface areas (SSAs) of ≈1200 $m^2\ g^{-1}$ (Figure S10 and Table S2, Supporting Information). These indicate uniform carbon coatings formed on the Al_2O_3 nanoparticles via catalytic CVD without severe restriction of CH_4 diffusion within the template pellets, regardless of the pellet densities. The total porosity (the sum of the micro-, meso-, and macroporosities) of the xN-20mg-4.0h-GMS-sheet, as calculated based on the areal density and thickness, is inversely related to the pelletization force (Figure 2d). This suggested that the pelletization force may mainly control the macroporosity, which cannot be detected via N_2 adsorption measurements. However, the mechanical strength of the GMS-sheets weaken when the pelletization force is smaller. As the 50 N-20 mg-4.0 h-GMS-sheet is not sufficiently rigid, we used the optimal pelletization force of 100 N in the subsequent experiments and further optimized the other parameters.

Generally, a carbon cathode with a large SSA may provide more active sites for Li_2O_2 formation, which is favorable in realizing a large capacity.[15] Thus, we attempted to increase the SSA by decreasing the duration of CVD, which is a key synthetic parameter in determining the average graphene-stacking number. As shown in Figure 2e,f, a CVD duration of 2 h provides a high BET SSA of ≈2000 $m^2\ g^{-1}$. The corresponding average graphene-stacking number is 1.5, based on the TG analysis (Figure S11, Supporting Information). Such a BET SSA is comparable to that of high-performance activated carbon,[20] whereas the ultra-high pore volume (>4.0 $cm^3\ g^{-1}$) is distinct. Moreover, the areal densities and the thicknesses of the GMS-sheets can be increased (Figure S8, Supporting Information) while maintaining identical micro-/mesoporosity (Figure 2f, Figure S12, Supporting Information), demonstrating the flexibility of the structure control from the nano- to the micrometer scale. We have developed an advanced temperature-programmed desorption (TPD) analysis up to 1800 °C that can accurately quantify the number of edge sites in carbon materials using the total amount of H_2O, CO, CO_2, and H_2 as an index.[23] Based on the edge-site-free property of the GMS-sheet, as confirmed via TPD analysis (Figure S13, Supporting Information), the high SSA of the GMS-sheet is mainly due to the graphene basal planes rather than the edge sites, which destabilize the carbon material in electrochemical systems. [24] The edge-site-free GMS-sheet with a high SSA may thus exhibit a superior stability.

2.2. Specific Capacities and Energy Densities of the GMS-Sheets

Cyclic voltammetry (CV) was performed with a stepwise expansion of the upper limit potential from 3.2 to 4.8 V (vs Li/Li^+) in 0.5 м lithium bis(trifluoromethanesulfonyl)imide (LiTFSI) dissolved in tetraethylene glycol dimethyl ether (TEGDME), denoted 500 electrolyte, to evaluate the electrochemical stability of the GMS-sheet. We examined the oxidation onset potential at which a noticeable current increase is observed. As shown in Figure S14 (Supporting Information) the GMS-sheet exhibits an onset potential of up to 4.6 V, which is higher than those of the CMS-sheet and a reference carbon nanotube sheet, indicating the superior electrochemical stability of the edge-site-free GMS-sheet.[24b]

Full-discharge–charge tests were performed in 0.5 м LiTFSI, 0.5 м lithium nitrate ($LiNO_3$), and 0.1 M 2,2,6,6-tetramethylpiperidinyloxyl (TEMPO) dissolved in TEGDME (denoted 551 electrolyte) using 2032-coin cells with components as shown in Figure S15 (Supporting Information). $LiNO_3$ effectively protects the Li metal anode,[25] and TEMPO acts as a redox mediator to reduce the charge potential.[11a,26] Twelve GMS-sheets synthesized under different conditions (Table S2, Supporting Information) were evaluated under a current density of 0.4 mA cm^{-2} with cut-off potentials of 2.0 and 4.5 V (vs Li/Li^+). All current densities were calculated based on the geometric area of GMS-sheet cathode (ϕ 12.5 mm, 1.23 cm^2). Note that a current density of 0.4 mAh cm^{-2} is a relatively high value compared to previous work, although a much higher current density can be used in Li-ion batteries. The Li–O_2 batteries display a discharge plateau at 2.65 V, as shown in **Figure 3**a,b. The initial specific capacities of Li–O_2 batteries were calculated by normalizing the full-discharge capacities to the geometric area and mass of the GMS-sheets (Table S3 and Note S2, Supporting Information). With a decrease in the pelletization force, the respective areal (Figure 3a) and mass (Figure S16a, Supporting Information) capacities increase significantly to >20.0 mAh cm^{-2} and >4500 mAh g^{-1} due to the increase in total porosity. Based on the data obtained for Nos. 8, 9, and 10, the smaller the graphene-stacking number, the larger the mass capacity (Figure S16b, Supporting Information), whereas the areal capacity remains almost identical (Figure 3b). Conversely, the larger the GMS-sheet cathode thickness, the larger was the areal discharge capacity (Figure 3b), whereas the mass discharge capacity remains almost identical (Figure S16b, Supporting Information). Figure 3c shows the relationship between the mass and areal capacities, which is controlled by three parameters: the pelletization force (porosity), amount of Al_2O_3 template (thickness), and duration of CVD (carbon layer). Notably, the 100N-30mg-2.0h-GMS-sheet (No. 12), as a practically heavy carbon cathode (> 4.0 mg cm^{-2}), displays ultra-high areal (>30.0 mAh cm^{-2}) and mass (>6200 mAh g^{-1}) capacities at a current density of 0.4 mA cm^{-2}, which affords the best performance compared to those reported in previous studies using other types of binder-free carbon cathodes (Figure 3d; Tables S3 and S4, Supporting Information).[10c,19a,27] We note that the competitive discharge capacities of GMS-sheets were achieved without the assistance of discharge catalysts. The addition of discharge catalysts, for example, 2,5-Di-tert-butyl-1,4-benzoquinone (DBBQ), may further improve the capacities.[27a,28]

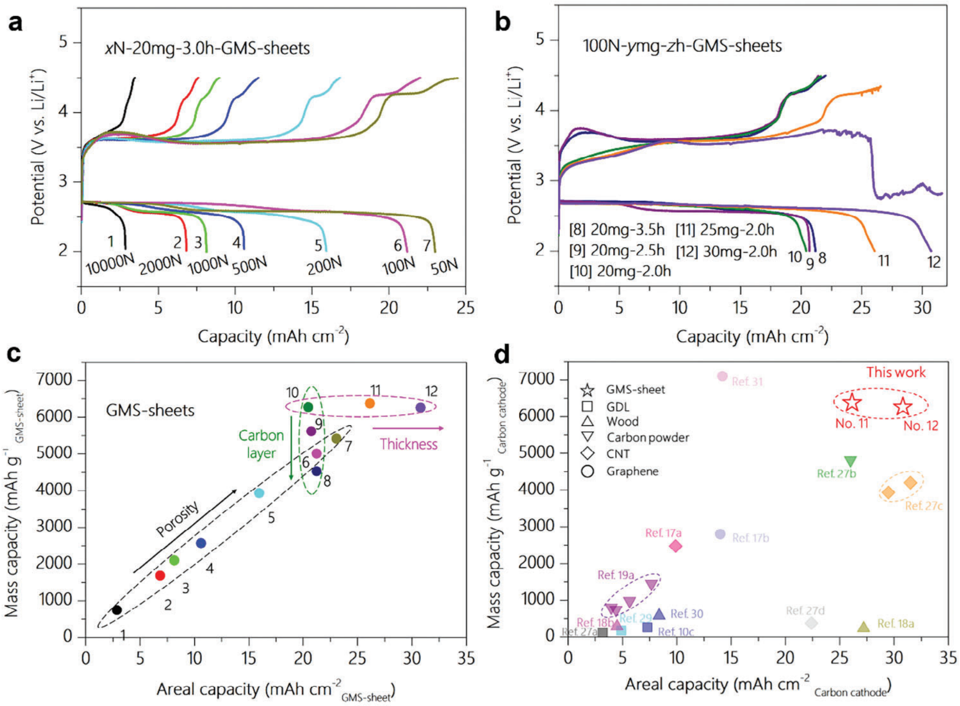

Figure 3. Full-discharge–charge measurements of GMS-sheets. Galvanostatic full-discharge–charge curves of Li–O_2 batteries based on GMS-sheets synthesized via various a) pelletization forces and b) Al_2O_3 amounts and durations of CVD. All the batteries were tested under a current density of 0.4 mA cm^{-2} and cut-off potentials of 2.0 and 4.5 V (vs Li/Li$^+$) with a 551 electrolyte. c) Mass and areal full-discharge capacities of twelve GMS-sheets shown in (a) and (b). d), Comparison of specific full-discharge mass and areal capacities with other representative published data. References with an areal weight of >1.0 mg cm^{-2} were selected.

Besides, volumetric energy density is also a critical performance parameter, particularly for practical batteries. In this study, a volumetric capacity of >450 mAh cm^{-3} could be obtained in high-porosity GMS-sheets (>95%) possibly due to their hierarchically porous structures (Figure S17a, Supporting Information). Besides, the battery with the 100N-30mg-2.0h-GMS-sheet (No. 12) displays a specific energy density of up to 793 Wh kg^{-1} (Figure S17a, Supporting Information) normalized to the total mass of all the active materials, including the Li metal, liquid electrolyte, GMS-sheet cathode, and discharge products (Li_2O_2) on the cathode.[13b,c] As summarized in Figure S17b and Table S4 (Supporting Information), GMS-sheets overperform the reported carbon materials, including a gas diffusion layer (GDL),[10c,27a,29] wood-derived carbon,[18,30] commercial carbon powder (mainly carbon black),[19a,27b] CNT,[17a,19b,27c,d] and graphene.[17b,31] Due to its superior performance in terms of specific energy density and mass, areal, and volumetric capacities, angstrom to sub-millimeter synthesis-controllable GMS-sheet is one of the most promising carbon cathodes for practical Li–O_2 batteries.

As to the charge process, a charge plateau below 3.7 V corresponds to the redox potential of TEMPO.[11a,27a] A sudden potential drop occurs at the end of charging (No. 12, Figure 3b), indicating a short circuit caused by the penetration of Li dendrites through the glass fiber separator in the first cycle owing to the ultra-high areal charge capacity (>30.0 mAh cm^{-2}).[32] Conventional Li–O_2 batteries are based on the balanced performances and stabilities of their components, including cathodes, separators, electrolytes, and anodes. The extremely high capacity of the 100N-30mg-2.0h-GMS-sheet causes the unexpected deterioration of other battery components in the typical configuration. This implies that the GMS-sheet significantly overperforms and the development of the other battery components is required to fully utilize the potential of the GMS-sheet.

2.3. Discharge–Charge Mechanism

To investigate the discharge–charge mechanism, GMS-sheets (100N-25mg-2.5h) at different discharge/charge stages were characterized via comprehensive ex situ and in situ techniques (Figure 4). As shown in **Figure 4a**, four Li–O_2 batteries were stopped after discharge for 10 h (10h-D), discharge for 30 h (30h-D), full-discharge to the lower cut-off potential (F-D), and full-discharge–charge to the upper cut-off potential (F-D-C), respectively. The GMS-sheet cathode is then removed from the battery and thoroughly washed with 1,2-dimethoxyethane (DME) to completely remove the electrolyte before further characterization (Figure S18, Supporting Information). The XRD patterns of the GMS-sheets after the battery tests reveal that the formation and decomposition of Li_2O_2 dominates the discharge–charge process (Figure S19, Supporting Information). Time-of-flight secondary ion mass spectrometry (TOF-SIMS) was used to obtain the depth distribution data of Li_2O_2 (LiO^- signals) within the various GMS-sheets after discharge–charge (Figure 4b). The signal in the 10h-D sample exhibits no clear change during the tests, with a consistently low intensity, which is possibly due to the uniform

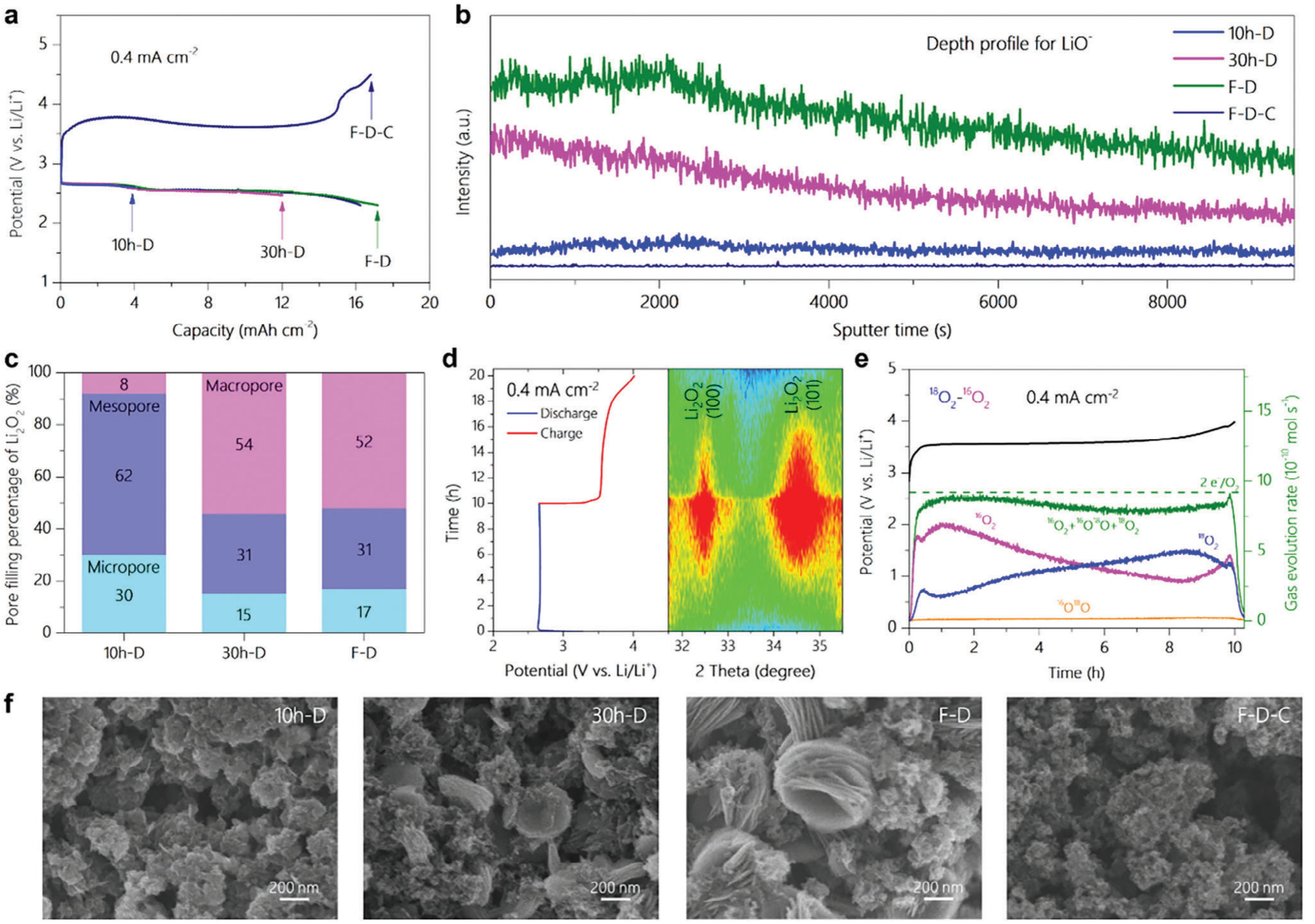

Figure 4. Mechanistic study of Li_2O_2 formation and decomposition in GMS-sheets. a) Galvanostatic discharge–charge curves of GMS-sheets with various cut-off conditions. A current density of 0.4 mA cm^{-2} was used for all four Li–O_2 batteries and the batteries were stopped after 10 h of discharge (10h-D), 30 h of discharge (30h-D), full-discharge to a cut-off potential of 2.3 V (F-D), and full-discharge–charge with a cut-off potentials of 2.3 and 4.5 V (F-D-C). GMS-sheets after discharge–charge were removed from the batteries stopped at certain conditions and washed three times with DME. b) Depth profiles of LiO^--signal in GMS-sheets after discharge—charge analyzed via TOF-SIMS. c) Comparison of Li_2O_2 occupation in micro-, meso-, and macropores of GMS-sheets, calculated from Figure S20a (Supporting Information). d) Discharge–charge curves of GMS-sheets and 2D color filled contour plot of in situ XRD patterns during the battery test under a current density of 0.4 mA cm^{-2} and a limited time of 10 h. e) Potential and gas evolution profiles during isotope DEMS test using GMS-sheet as a cathode. The battery was first discharged under isotope $^{18}O_2$ atmosphere for 5 h followed by another (5 h) discharge under $^{16}O_2$ atmosphere with a current density of 0.4 mA cm^{-2}. f) SEM images of the gas/electrode interfaces of four GMS-sheets after discharge–charge as shown in Figure 4a.

formation of Li_2O_2 around the abundant mesopores of the GMS-sheet at the early stage of the discharge. The gradually decreasing signals in the 30h-D and F-D samples with sputtering time indicate the accumulation of Li_2O_2 on the exterior of the GMS-sheet,[33] which suggests a different Li_2O_2 formation mechanism in the macropores at the later stage. As evidenced by the N_2 ad-/desorption isotherms (Figure S20, Supporting Information), the GMS-sheets maintain their hierarchically porous structures even after discharge, but the micro-/mesopores decrease during discharge and then recover after the charge. As shown in Figure 4c and Table S6 (Supporting Information), most of the Li_2O_2 (92%) is formed in the micro-/mesopores at the beginning of the discharge (10h-D), but >50% of the Li_2O_2 occupies the macropores with increasing discharge time (30h-D and F-D). Remarkably, the ratios of the percentages of Li_2O_2 in the micro- and mesopores of the GMS-sheets are almost the same (1:2) at different discharge stages, which may be related to the uniform nucleation of Li_2O_2 on the surface of the graphene framework.[34]

In situ XRD of the GMS-sheet cathode during discharge and charge were performed in a Li–O_2 battery using the 0.5 M LiTFSI, 0.5 M $LiNO_3$, and 0.2 M lithium bromide (LiBr) dissolved in TEGDME (denoted 552 electrolyte), where the dominant reactions are still the formation and decomposition of Li_2O_2 (Figure S21, Supporting Information). As shown in the contour plot (Figure 4d), clear diffraction signals representing the (100) and (101) facets of Li_2O_2 are observed after 4 h, corresponding to a discharge capacity of 1.6 mAh cm^{-2}. These signals are no longer observed after charging for 6 h (4 h to the end). To further clarify the mechanism of Li_2O_2 decomposition on the GMS-sheet, differential electrochemical mass spectrometry (DEMS) was performed using $^{18}O_2$/$^{16}O_2$ isotope (Figure 4e). Discharge is initially performed in an $^{18}O_2$ atmosphere for 5 h and then in a $^{16}O_2$

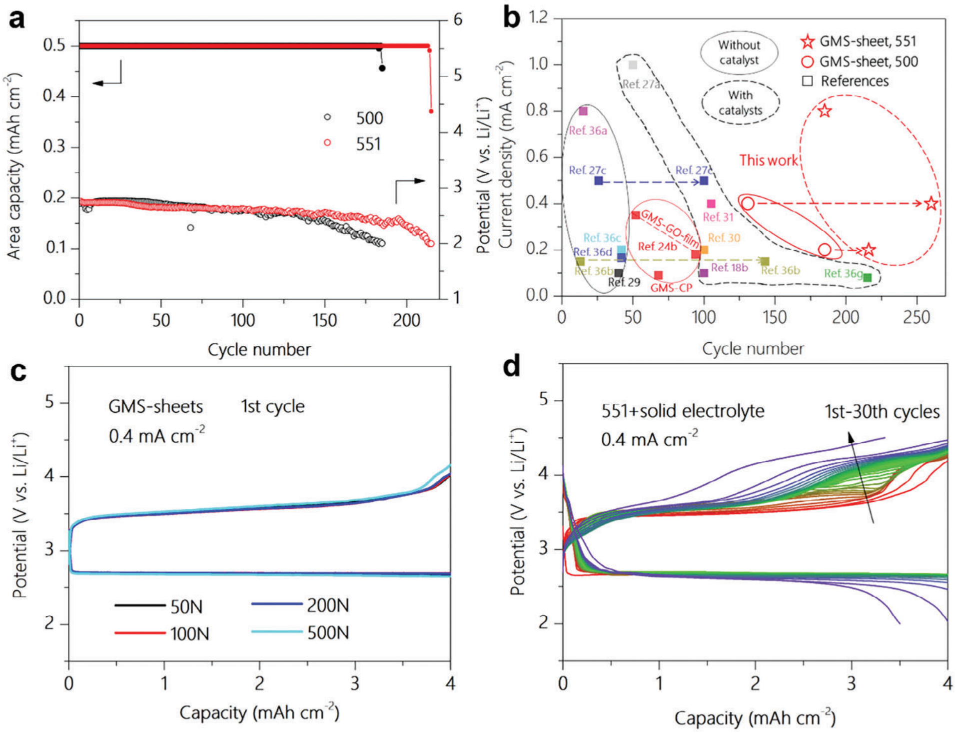

Figure 5. Cycle stabilities of GMS-sheets in Li–O_2 batteries. a) Long-cycle stability of GMS-sheet-based Li–O_2 batteries using 500 and 551 electrolytes at a respective current density and limited capacity of 0.2 mA cm^{-2} and 0.5 mAh cm^{-2}. b) Comparison of current densities and cycle stability with other representative published data. The reference numbers and detailed parameters in b are listed in Table S7 (Supporting Information). c) The 1st galvanostatic discharge–charge curves and d) Galvanostatic discharge–charge curves of a Li–O_2 battery containing a solid electrolyte. All the batteries in c and d were evaluated at a respective current density and limited capacity of 0.4 mA cm^{-2} and 4.0 mAh cm^{-2}.

atmosphere for another 5 h at a current density of 0.4 mA cm^{-2}. The second supplied oxygen, $^{16}O_2$, is detected as the O_2 at the beginning of charging, suggesting that Li_2O_2 decomposition possibly occurs at the Li_2O_2/electrolyte interface.[35] In addition, the total O_2 evolution amount is close to the theoretical line of the two-electron transfer reaction throughout charging, indicating the efficient decomposition of Li_2O_2 within the GMS-sheet.

SEM images show the morphological changes of Li_2O_2 on the surface (Figure 4f) and inside the GMS-sheet (Figure S22, Supporting Information) during the discharge–charge. As shown in Figure 4f, the average particle size of Li_2O_2 on the outer surface (close to air) gradually increases throughout discharging, from <100 nm (10h-D) to 300 (30h-D) and then to 800 nm (F-D). In comparison, the Li_2O_2 formed inside the GMS-sheets displays a limited size of 300 nm owing to spatial confinement (Figure S22a, Supporting Information). Based on the characterization results (Figure 4b–f), a possible mechanism is proposed, as shown in Figure S22b (Supporting Information). In short, the discharge process follows a mechanism of nucleation within the micro-/mesopores and growth in the macropores, and the charge process corresponds to the typical decomposition of Li_2O_2 by redox mediators. Therefore, the excellent battery performance is strongly related to the unique discharge–charge mechanism in a GMS-sheet with a hierarchically porous structure.

2.4. Cycle Stability

The stability of Li–O_2 batteries using GMS-sheets (100N-25mg-4.0h) with an areal density of 6.5 mg cm^{-2} was first examined in the 500 and 551 electrolytes using a medium current density of 0.2 mA cm^{-2} and a limited capacity of 0.5 mAh cm^{-2}. The number of cycles is defined as the maximum number of cycles that the discharge process can contribute to a limited capacity of 0.5 mAh cm^{-2} before the potential reaches a cut-off potential of 2.0 V (V vs Li/Li^{+}). As shown in **Figure 5a**, the GMS-sheet exhibits a superior cycle stability (185 cycles) in the 500 electrolytes, even without solid/soluble catalysts. The cycle life of the GMS-sheet increases to 216 cycles (>1080 h, Figure S23, Supporting Information) in the 551 electrolytes. In addition to the excellent oxidation resistance of the GMS-sheet (Figure S14, Supporting Information), the charging process could be much cleaner by reducing the charging overpotential using redox mediators. This is supported by the increased O_2 evolution amount close to the theoretical line of 2-electron transfer and the suppressed CO_2 evolution during DEMS test using the 551-electrolytes (Figure S24, Supporting Information). Moreover, the GMS-sheet shows an excellent rate performance at a current density of 0.1–0.8 mA cm^{-2} in the 551-electrolyte (Figure S25, Supporting Information). The GMS-sheet shows 260 cycles at 0.4 mA cm^{-2} and 185 cycles at 0.8 mA cm^{-2} in the 551-electrolytes (Figure S26, Supporting Information), demonstrating the excellent rate performance and superior cycle stability. Note that despite the upper limited potential of 4.8 V (V vs Li/Li^+) being set, the charge potential is <4.6 V (V vs Li/Li^+) except for the last few cycles, which is a relatively safe potential for GMS-sheets (Figure S14a, Supporting Information). We compared the cycle stabilities of the GMS-sheet and representative carbon cathodes reported in previous studies (Table S7, Supporting Information).[18b,24b,27a,29–31,36] As summarized in Figure 5b, without any solid or soluble catalysts (solid circles), the binder-free GMS-sheet outperforms state-of-the-art carbon cathodes.[24b] Similar to previous reports, the cycle life was enhanced by adding a mediator (TEMPO in this study, dash circles in Figure 5b). Interestingly, adding the mediator at a lower current of 0.2 mA cm^{-2} does not significantly improve battery cycle stability (from 185 to 216 cycles), as opposed to the case with a higher current density of 0.4 mA cm^{-2} (from 130 to 260 cycles). This result indicates the necessity of both a stable GMS-sheet cathode and a mediator when operating at a high current density.

Finally, the cycle stability of GMS-sheets was estimated in $Li–O_2$ batteries with a current density of 0.4 mA cm^{-2} and a limited capacity of 4.0 mAh cm^{-2} (615 mAh g^{-1}). We note that the capacity of 4.0 mAh cm^{-2} is much higher than conventional values (<1.0 mAh cm^{-2}) used as limited capacities in previous work.[13b] As shown in Figure 5c, four high-porosity GMS-sheets exhibit similar high-potential discharge plateau (2.75 V) and low-potential charge plateau (3.5 V), corresponding to a high energy efficiency of 78%.[13b] All the GMS-sheets worked well during the first 10 cycles (Figure S27, Supporting Information), but during the following cycles, all batteries experienced a sudden potential drop during the charge process, possibly owing to precipitous short circuit caused by Li dendrite.[32] The Li dendrite problem is alleviated by introducing an additional polypropylene (PP) membrane on the Li anode side, and the battery life is extended to 16 cycles (Figure S27, Supporting Information). Hence, the GMS-sheets are sufficiently stable as high-performance cathodes, and other factors cause battery death. To further improve the cycle performance, a solid electrolyte (lithium-ion conducting glass-ceramics, LICGC, Ohara) was introduced into the battery to inhibit the shuttle effect, wherein the byproducts formed at the cathode migrate to the Li anode and induce its deterioration.[37] Consequently, stable cycling up to 30 cycles is achieved (Figure 5d), which is one of the best cycle performances using a current density of 0.4 mA cm^{-2} and large limited capacity of 4.0 mAh cm^{-2} .[17a,19a,27b,c] The stable cycling performance (19 cycles) of the $Li–O_2$ battery based on the solid electrolyte and the 552-electrolyte also proves the stability of the GMS-sheet (Figure S28, Supporting Information), and the major cause of battery death is not the GMS-sheet cathode but other battery components, including the electrolyte and anode. Thus, $Li–O_2$ batteries with improved cyclability can be constructed by combining a GMS-sheet cathode with other advanced techniques and materials.[10b,38] For perspective, the GMS sheet with a hierarchical porous structure can potentially be used in other metal–gas batteries, especially in nonaqueous systems, given the hydrophobicity of the GMS sheet (Figure S29, Supporting Information). For example, a nonaqueous $Na–O_2$ battery based on a 100N-25mg-2.5h-GMS-sheet cathode also works well in a limited capacity cycle and shows lower overpotential in the first cycle compared to a CNT-film cathode (Figure S30, Supporting Information).

3. Conclusion

We report synthesis of a binder-free GMS-sheet cathode with a controllable size on the angstrom to submillimeter scale and a hierarchical porous graphene-wall structure for practical $Li–O_2$ batteries with high energy densities. By optimizing the pelletization force, template amount, and duration of CVD, high-porosity (>95%) GMS-sheets with high surface area of >2000 m^2 g^{-1} and large pore volume up to 4.54 cm^3 g^{-1} were synthesized. Using these GMS-sheets as practical cathodes (>4.0 mg cm^{-2}), $Li–O_2$ batteries simultaneously exhibited an ultra-large areal (>30.0 mAh cm^{-2}), mass (>6300 mAh g^{-1}), and volumetric (>480 mAh cm^{-3}) capacities. The $Li–O_2$ battery with the optimized GMS-sheet cathode displayed the optimal energy densities of 793 (normalized by all active materials, electrolytes, and Li_2O_2) and 2609 Wh kg^{-1} (normalized by GMS-sheet and Li_2O_2). Comprehensive characterization demonstrated that the high specific capacity of the GMS-sheet was attributable to its precisely controlled hierarchical structure. The outstanding rate performance and cycle stability tested at a current density of 0.4 mA cm^{-2}) and limited capacity of 4.0 mAh cm^{-2} prove that the GMS-sheet is a promising carbon cathode for practical $Li–O_2$ batteries. This study demonstrates that a proper structural design of carbon cathode may overcome most of the major issues of $Li–O_2$ battery cathodes. The optimized carbon cathode is no longer a bottleneck of $Li–O_2$ batteries in terms of energy density and cyclability. In the future, large-scale synthesis of the hierarchical high-porosity GMS-sheet cathode with a practical pouch-cell size should promote the commercialization of practical $Li–O_2$ batteries with high energy density.

Supporting Information

Supporting Information is available from the Wiley Online Library or from the author.

Acknowledgements

This work was supported by the JST ALCA-SPRING, Japan (grant no. JPMJAL1301), the JSPS KAKENHI (grant nos. 22K14757 and 21K14490), and the JST SICORP Grant no. JPMJSC2112.

Conflict of Interest

The authors declare no competing interests.

Author Contributions

W.Y. and H.N. conceived the idea, designed the experiments, and wrote the manuscript, and H.N. directed the project. W.Y. and Z.H.S. synthesized the GMS-sheets. Z.H.S. performed the TEM tests. W.Y. conducted the battery tests, the SEM tests, the N_2 adsorption/desorption tests, the TPD tests and the Raman tests. W.Y. and T.Y. and A.A. performed the TOF-SIMS. W.Y., S.M., and S.N. performed DEMS tests and battery tests with a solid electrolyte. M.A. and T.K. performed in situ XRD tests. W.Y., S.I., and S.R.M. conducted BET tests. All authors discussed and analyzed the data.

Data Availability Statement

The data that support the findings of this study are available from the corresponding author upon reasonable request.

Keywords

carbon cathodes, graphene mesosponges, hierarchical structure, lithium–oxygen batteries

Received: September 12, 2023
Revised: October 16, 2023
Published online: November 10, 2023

---

[1] T. Liu, J. P. Vivek, E. W. Zhao, J. Lei, N. Garcia-Araez, C. P. Grey, *Chem. Rev.* **2020**, *120*, 6558.

[2] P. G. Bruce, S. A. Freunberger, L. J. Hardwick, J.-M. Tarascon, *Nat. Mater.* **2012**, *11*, 19.

[3] J. Lu, Y. Jung Lee, X. Luo, K. Chun Lau, M. Asadi, H.-H. Wang, S. Brombosz, J. Wen, D. Zhai, Z. Chen, D. J. Miller, Y. Sub Jeong, J.-B. Park, Z. Zak Fang, B. Kumar, A. Salehi-Khojin, Y.-K. Sun, L. A. Curtiss, K. Amine, *Nature* **2016**, *529*, 377.

[4] T. Liu, M. Leskes, W. Yu, A. J. Moore, L. Zhou, P. M. Bayley, G. Kim, C. P. Grey, *Science* **2015**, *350*, 530.

[5] a) A. Kondori, M. Esmaeilirad, A. M. Harzandi, R. Amine, M. T. Saray, L. Yu, T. Liu, J. Wen, N. Shan, H.-H. Wang, A. T. Ngo, P. C. Redfern, C. S. Johnson, K. Amine, R. Shahbazian-Yassar, L. A. Curtiss, M. Asadi, *Science* **2023**, *379*, 499; b) C. Xia, C. Y. Kwok, L. F. Nazar, *Science* **2018**, *361*, 777.

[6] X. Chi, M. Li, J. Di, P. Bai, L. Song, X. Wang, F. Li, S. Liang, J. Xu, J. Yu, *Nature* **2021**, *592*, 551.

[7] W.-J. Kwak, Rosy, D. Sharon, C. Xia, H. Kim, L. R. Johnson, P. G. Bruce, L. F. Nazar, Y.-K. Sun, A. A. Frimer, M. Noked, S. A. Freunberger, D. Aurbach, *Chem. Rev.* **2020**, *120*, 6626.

[8] a) N. B. Aetukuri, B. D. Mccloskey, J. M. García, L. E. Krupp, V. Viswanathan, A. C. Luntz, *Nat. Chem.* **2015**, *7*, 50; b) L. Johnson, C. Li, Z. Liu, Y. Chen, S. A. Freunberger, P. C. Ashok, B. B. Praveen, K. Dholakia, J.-M. Tarascon, P. G. Bruce, *Nat. Chem.* **2014**, *6*, 1091; c) D. Aurbach, B. D. Mccloskey, L. F. Nazar, P. G. Bruce, *Nat. Energy* **2016**, *1*, 16128; d) L. Luo, B. Liu, S. Song, W. Xu, J.-G. Zhang, C. Wang, *Nat. Nanotechnol.* **2017**, *12*, 535.

[9] a) S. Wu, J. Yi, K. Zhu, S. Bai, Y. Liu, Y. Qiao, M. Ishida, H. Zhou, *Adv. Energy Mater.* **2017**, *7*, 1601759; b) Z. Huang, J. Ren, W. Zhang, M. Xie, Y. Li, D. Sun, Y. Shen, Y. Huang, *Adv. Mater.* **2018**, *30*, 1803270.

[10] a) B. Tong, J. Huang, Z. Zhou, Z. Peng, *Adv. Mater.* **2018**, *30*, 1704841; b) Y. Qiao, Q. Wang, X. Mu, H. Deng, P. He, J. Yu, H. Zhou, *Joule* **2019**, *3*, 2986; c) X. Gao, Y. Chen, L. Johnson, P. G. Bruce, *Nat. Mater.* **2016**, *15*, 882.

[11] a) B. J. Bergner, A. Schürmann, K. Peppler, A. Garsuch, J. Janek, *J. Am. Chem. Soc.* **2014**, *136*, 15054; b) H.-D. Lim, B. Lee, Y. Zheng, J. Hong, J. Kim, H. Gwon, Y. Ko, M. Lee, K. Cho, K. Kang, *Nat. Energy* **2016**, *1*, 16066.

[12] a) M. M. Ottakam Thotiyl, S. A. Freunberger, Z. Peng, P. G. Bruce, *J. Am. Chem. Soc.* **2013**, *135*, 494; b) M. M. Ottakam Thotiyl, S. A. Freunberger, Z. Peng, Y. Chen, Z. Liu, P. G. Bruce, *Nat. Mater.* **2013**, *12*, 1050.

[13] a) H. C. Lee, J. O. Park, M. Kim, H. J. Kwon, J.-H. Kim, K. H. Choi, K. Kim, D. Im, *Joule* **2019**, *3*, 542; b) Z. Liang, W. Wang, Y.-C. Lu, *Joule* **2022**, *6*, 2458; c) C. Prehal, S. A. Freunberger, *Joule* **2019**, *3*, 321.

[14] K. G. Gallagher, S. Goebel, T. Greszler, M. Mathias, W. Oelerich, D. Eroglu, V. Srinivasan, *Energy Environ. Sci.* **2014**, *7*, 1555.

[15] M. Balaish, J.-W. Jung, I.-D. Kim, Y. Ein-Eli, *Adv. Funct. Mater.* **2020**, *30*, 1808303.

[16] J.-H. Kang, J. Lee, J.-W. Jung, J. Park, T. Jang, H.-S. Kim, J.-S. Nam, H. Lim, K. R. Yoon, W.-H. Ryu, I.-D. Kim, H. R. Byon, *ACS Nano* **2020**, *14*, 14549.

[17] a) S. H. Park, Y. J. Cheon, Y. J. Lee, K. H. Shin, Y. Y. Hwang, Y. S. Jeong, Y. J. Lee, *ACS Appl. Mater. Interfaces* **2019**, *11*, 30872; b) Y. Lin, B. Moitoso, C. Martinez-Martinez, E. D. Walsh, S. D. Lacey, J.-W. Kim, L. Dai, L. Hu, J. W. Connell, *Nano Lett.* **2017**, *17*, 3252.

[18] a) C. Chen, S. Xu, Y. Kuang, W. Gan, J. Song, G. Chen, G. Pastel, B. Liu, Y. Li, H. Huang, L. Hu, *Adv. Energy Mater.* **2019**, *9*, 1802964; b) H. Song, S. Xu, Y. Li, J. Dai, A. Gong, M. Zhu, C. Zhu, C. Chen, Y. Chen, Y. Yao, B. Liu, J. Song, G. Pastel, L. Hu, *Adv. Energy Mater.* **2017**, *8*, 1701203.

[19] a) J. Saengkaew, T. Kameda, M. Ono, S. Matsuda, *Mater. Adv.* **2022**, *3*, 3536; b) Y. Wu, B. Zhao, X. Zhao, L. Han, Y. Shang, Z. Niu, Y. Liang, X. Zhang, Z. Jiang, F. Li, A. Cao, *Mater. Today* **2022**, *59*, 68.

[20] H. Nishihara, T. Simura, S. Kobayashi, K. Nomura, R. Berenguer, M. Ito, M. Uchimura, H. Iden, K. Arihara, A. Ohma, Y. Hayasaka, T. Kyotani, *Adv. Funct. Mater.* **2016**, *26*, 6418.

[21] a) C. Xu, P. Behrens, P. Gasper, K. Smith, M. Hu, A. Tukker, B. Steubing, *Nat. Commun.* **2023**, *14*, 119; b) J. Huang, S. T. Boles, J.-M. Tarascon, *Nat. Sustain.* **2022**, *5*, 194.

[22] S. Sunahiro, K. Nomura, S. Goto, K. Kanamaru, R. Tang, M. Yamamoto, T. Yoshii, J. N. Kondo, Q. Zhao, A. Ghulam Nabi, R. Crespo-Otero, D. Di Tommaso, T. Kyotani, H. Nishihara, *J. Mater. Chem. A* **2021**, *9*, 14296.

[23] a) T. Ishii, S. Kashihara, Y. Hoshikawa, J.-I. Ozaki, N. Kannari, K. Takai, T. Enoki, T. Kyotani, *Carbon* **2014**, *80*, 135; b) Y. Tao, X. Xie, W. Lv, D.-M. Tang, D. Kong, Z. Huang, H. Nishihara, T. Ishii, B. Li, D. Golberg, F. Kang, T. Kyotani, Q.-H. Yang, *Sci. Rep.* **2013**, *3*, 2975.

[24] a) Y. Bae, Y. S. Yun, H.-D. Lim, H. Lee, Y.-J. Kim, J. Kim, H. Park, Y. Ko, S. Lee, H. J. Kwon, H. Kim, H.-T. Kim, D. Im, K. Kang, *Chem. Mater.* **2016**, *28*, 8160; b) W. Yu, T. Yoshii, A. Aziz, R. Tang, Z.-Z. Pan, K. Inoue, M. Kotani, H. Tanaka, E. Scholtzová, D. Tunega, Y. Nishina, K. Nishioka, S. Nakanishi, Y. Zhou, O. Terasaki, H. Nishihara, *Adv. Sci.* **2023**, *10*, 2300268.

[25] a) C. M. Burke, V. Pande, A. Khetan, V. Viswanathan, B. D. Mccloskey, *Proc. Natl. Acad. Sci. USA* **2015**, *112*, 9293; b) Y. Yu, G. Huang, J.-Y. Du, J.-Z. Wang, Y. Wang, Z.-J. Wu, X.-B. Zhang, *Energy Environ. Sci.* **2020**, *13*, 3075.

[26] a) Z. Liang, Q. Zou, J. Xie, Y.-C. Lu, *Energy Environ. Sci.* **2020**, *13*, 2870; b) X. Wu, W. Yu, K. Wen, H. Wang, X. Wang, C.-W. Nan, L. Li, *J Energy Chem* **2021**, *60*, 135.

[27] a) X. Gao, Y. Chen, L. R. Johnson, Z. P. Jovanov, P. G. Bruce, *Nat. Energy* **2017**, *2*, 17118; b) S. Matsuda, E. Yasukawa, T. Kameda, S. Kimura, S. Yamaguchi, Y. Kubo, K. Uosaki, *Cell Rep Phys Sci.* **2021**, *2*, 100506; c) Y. J. Lee, S. H. Park, S. H. Kim, Y. Ko, K. Kang, Y. J. Lee, *ACS Catal.* **2018**, *8*, 2923; d) W. Chen, W. Yin, Y. Shen, Z. Huang, X. Li, F. Wang, W. Zhang, Z. Deng, Z. Zhang, Y. Huang, *Nano Energy* **2018**, *47*, 353.

[28] Y. Gao, Z. Yan, J. L. Gray, X. He, D. Wang, T. Chen, Q. Huang, Y. C. Li, H. Wang, S. H. Kim, T. E. Mallouk, D. Wang, *Nat. Mater.* **2019**, *18*, 384.

[29] J. Zhang, B. Sun, Y. Zhao, A. Tkacheva, Z. Liu, K. Yan, X. Guo, A. M. Mcdonagh, D. Shanmukaraj, C. Wang, T. Rojo, M. Armand, Z. Peng, G. Wang, *Nat. Commun.* **2019**, *10*, 602.

[30] C. Zhu, L. Du, J. Luo, H. Tang, Z. Cui, H. Song, S. Liao, *J. Mater. Chem. A* **2018**, *6*, 14291.

[31] W.-B. Luo, S.-L. Chou, J.-Z. Wang, Y.-C. Zhai, H.-K. Liu, *Small* **2015**, *11*, 2817.

[32] W. Yu, C. Xue, B. Hu, B. Xu, L. Li, C.-W. Nan, *Energy Storage Mater.* **2020**, *27*, 244.

[33] C. Tan, D. Cao, L. Zheng, Y. Shen, L. Chen, Y. Chen, *J. Am. Chem. Soc.* **2022**, *144*, 807.

[34] S. Lau, L. A. Archer, *Nano Lett.* **2015**, *15*, 5995.

[35] a) K. Nishioka, K. Morimoto, T. Kusumoto, T. Harada, K. Kamiya, Y. Mukouyama, S. Nakanishi, *J. Am. Chem. Soc.* **2021**, *143*,

7394; b) K. Nishioka, M. Tanaka, H. Fujimoto, T. Amaya, S. Ogoshi, M. Tobisu, S. Nakanishi, *Angew. Chem., Int. Ed.* **2022**, *61*, e202112769.

[36] a) Z. Liang, Y.-C. Lu, *J. Am. Chem. Soc.* **2016**, *138*, 7574; b) X. Lin, Z. Sun, C. Tang, Y. Hong, P. Xu, X. Cui, R. Yuan, Z. Zhou, M. Zheng, Q. Dong, *Adv. Energy Mater.* **2020**, *10*, 2001592; c) B. Zhou, L. Guo, Y. Zhang, J. Wang, L. Ma, W.-H. Zhang, Z. Fu, Z. Peng, *Adv. Mater.* **2017**, *29*, 1701568; d) C. Yu, C. Zhao, S. Liu, X. Fan, J. Yang, M. Zhang, J. Qiu, *Chem. Commun.* **2015**, *51*, 13233; e) J.-W. Jung, D.-W. Choi, C. K. Lee, K. R. Yoon, S. Yu, J. Y. Cheong, C. Kim, S.-H. Cho, J.-S. Park, Y. J. Park, I.-D. Kim, *Nano Energy* **2018**, *46*, 193; f) C. Y. Jung, T. S. Zhao, L. Zeng, P. Tan, *J. Power Sources* **2016**, *331*, 82; g) X. Zhu, Y. Shang, Y. Lu, C. Liu, Z. Li, Q. Liu, *J. Power Sources* **2020**, *471*, 228444.

[37] S. Matsuda, M. Ono, H. Asahina, S. Kimura, E. Mizuki, E. Yasukawa, S. Yamaguchi, Y. Kubo, K. Uosaki, *Adv. Energy Mater.* **2023**, *13*, 2203062.

[38] a) Y. Ko, H. Park, K. Lee, S. J. Kim, H. Park, Y. Bae, J. Kim, S. Y. Park, J. E. Kwon, K. Kang, *Angew. Chem., Int. Ed.* **2020**, *59*, 5376; b) Q. Han, W. Guo, X. He, T. Liu, X. Liu, X. Zhu, T. Bian, L. Jiang, J. Lu, Y. Zhao, *Joule* **2022**, *6*, 381.